Design and analysis of magnetostrictive sensors for wireless temperature sensing

Manjunath C. Rajagopal and Sanjiv Sinha (sanjiv@illinois.edu)

Department of Mechanical Science and Engineering

University of Illinois at Urbana-Champaign, Urbana, IL 61801, USA.

Abstract

Magnetostrictive transducers are commonly used as actuators, sonar transducers, and in remote non-destructive evaluation. Their use in wireless thermometry is relatively unexplored. Since magnetostriction-based sensors are passive, they could potentially enable long-term near-field thermometry. While the temperature sensitivity of resonance frequency in magnetostrictive transducers has been reported in previous studies, the origin of the temperature sensitivity has however not been elucidated. Here, we identify material properties that determine temperature sensitivity, and identify ways to improve sensitivity as well as the detection technique. Using a combination of analytical and computational methods, we systematically identify the material properties that directly influence the temperature coefficient of resonance frequency (TCF). We first experimentally measure the shift in resonance frequency due to temperature changes in a Metglas strip to be 0.03%K^{-1}. Using insights from theory, we then experimentally demonstrate a 5-fold improvement to the TCF by using Terfenol in place of Metglas as the magnetostrictive sensor material. We further demonstrate an alternate temperature sensing technique that does not require measuring the resonance frequency, consequently reducing instrument complexity. This work provides a general framework to analyze magnetostrictive materials and the sensing scheme for near-field wireless thermometry.

I. Introduction

Wireless temperature sensing has enabled applications such as environmental temperature monitoring [1], [2], data center cooling monitoring [2], [3], core body temperature measurements [4], etc. Such techniques typically involve RFID tags [5], [6], LC circuits [7], [8], SAW resonators

[9], [10], etc., which require extensive fabrication [11], [12], high instrument complexity [5], [13], and rigorous signal decoding techniques [1], [9]. Here, we explore magnetostrictive transducers as a potential alternative for near-field wireless thermometry. Magnetostrictive materials respond to an excitation magnetic flux by deforming mechanically, initiating an elastic wave in the material. In turn, the elastic wave induces a magnetic flux, which reaches a peak when the excitation magnetic flux is modulated at the natural mechanical frequency of the transducer. Thus, a coil near a magnetostrictive material can provide a direct electrical readout of the sensing parameter, which has enabled several low-cost [14], [15] applications such as anti-theft tags [16], food package tagging [17], fluid property measurements [18], etc. For instance, magnetostrictive transducers have been used for fluid property measurements such as pressure [18], [19], velocity [18], [20], viscosity [21], [22], humidity [18], [23], etc., and in industrial applications such as positioning actuators [24], sonar transducers [25], torque sensors [26], etc. Typical fluid properties such as pressure, viscosity, etc. affect the loading and/or damping of a resonating magnetostrictive sensor, which changes its resonance frequency [27]. On the other hand, temperature changes affect the intrinsic material properties, especially the Young's modulus of the magnetostrictive material [27], which results in a resonance frequency shift. While the temperature sensitivity of resonance frequency in magnetostrictive transducers has been reported in previous studies [23], [27]–[29], the origin of the temperature sensitivity has however not been elucidated.

There has been a growing interest in understanding the temperature dependence of the Young's modulus in magnetostrictive materials [29]–[33]. Previous work [29] used a simplified constitutive model to propose that the temperature-dependent anisotropy field could be the cause for the temperature dependence of Young's modulus. However, the anisotropy field's temperature dependence has neither been quantified nor been used to demonstrate any improvement to the temperature sensitivity. Recent studies [30]–[33] have provided more detailed non-linear constitutive models that utilize fundamental material properties in modeling the Young's modulus as a function of temperature and bias fields. Such studies [30]–[33] report on thermo-magneto-mechanical modeling of magnetostrictive materials, but lack direct experimental validation. Therefore, there is a need for systematic identification of new materials and/or new detection techniques that improve the sensitivity of magnetostrictive sensors to temperature changes.

In this work, we modify previously reported non-linear constitutive equations [30], and use them to both analytically and computationally model a magnetostriction-based temperature sensor.

We perform a sensitivity analysis, and experimentally demonstrate a 5-fold improvement to the temperature coefficient of resonance frequency (TCF). Such a wireless temperature measurement can be integrated into existing magnetostriction based actuators or transducers, which are currently used in applications such as high-pressure pipelines [34], drilling rigs [35], food packaging [17], [36], anti-theft tags [16], etc. The paper is organized as follows. In Section II, we report the thermo-magneto-mechanical constitutive equations and lumped circuit model that can model the TCF and capture the influence of different material properties. In Section III, we describe our experimental setup, which we use to measure the TCF of Metglas. Using the experimental results, in Section IV, we perform a sensitivity analysis to identify the material properties that determine temperature sensitivity. We use finite element simulations to study the influence of sensor dimensions. In Section V, we demonstrate an improvement to the TCF using Terfenol. We also discuss an alternative sensing technique that does not require measuring the resonance frequency to measure temperature changes. Overall, our work provides ways to improve the sensitivity and explores alternate measurement techniques for temperature sensing through new or repurposed existing magnetostrictive sensors.

II. Modelling

We model magnetostrictive transducers to gain insights that can be used to improve the sensitivity and detection technique for thermometry applications. First, we develop constitutive equations to predict the resonance frequency shift with temperature. Then, we develop a lumped circuit model to predict the induced voltage at a pickup coil. We describe our experimental setup in detail in Section III. Briefly, the magnetostrictive sensor strip is placed inside two concentric coils – one for bias and the other for sensing. The resonance frequency of a magnetostrictive sensor can be approximated to that of a free-standing thin-film, and is given by [37],

$$f_{res} = \frac{1}{2L}\sqrt{\frac{E}{\rho(1-\nu)}} \tag{1}$$

where, L is the length of the sensor, ρ is the density, ν is the Poisson's ratio, and E is the Young's modulus. The sensitivity to temperatures can be defined through the temperature coefficient of resonance frequency (TCF) which is $\Delta f/(\Delta T.f_o)$, where Δf is the change in resonance frequency from f_0 due to a change in temperature ΔT from T_0. In Section II a, we introduce constitutive equations that can be used to model the TCF for a magnetostrictive material. In Section II b, we develop a lumped circuit model that can provide insight into the detection technique, especially on the influence of sensor dimensions.

II. a. Thermo-magneto-mechanical model (static analysis)

In this Section, we discuss thermo-magneto-mechanical constitutive equations that can capture the experimentally observed variation in the resonance frequency of magnetostrictive sensors due to changes in bias fields and temperatures. The Young's modulus of magnetostrictive materials are typically a function of the applied magnetic field (H), the film stress (σ), temperature (T), and the magnetostrictive strain (λ). The relationship between the induced strain (ϵ), magnetization (M), and the applied magnetic field (H) has been analytically modeled in 1D in previous work [30]. We use a modified version of this analytical model, which we describe in the supplementary section. We show in the supplementary section that this analytical model can predict the experimentally measured magnetostrictive strain (λ) due to an applied magnetic field (H) for a variety of magnetostrictive materials such as Terfenol, Metglas 2605, 2801, etc. (Supplementary Figure S3). We extend this model as shown in Eqns. (2)-(3) to predict the Young's modulus of the magnetostrictive material under an applied dc magnetic field (H) and for small temperature changes ΔT from room temperature.

$$\frac{1}{E} = \frac{1}{E_s\,(1+\gamma\Delta T)} + \left(1-\frac{M^2}{M_s^2}\right)\frac{\lambda_s}{\sigma_s}\operatorname{sech}^2\left(\frac{2\sigma}{\sigma_s}\right) + \left(2-\tanh\left(\frac{2\sigma}{\sigma_s}\right)\right)\frac{\lambda_s M}{M_s^2}\frac{\partial M}{\partial \sigma} \qquad (2)$$

$$\frac{\partial M}{\partial \sigma} = \frac{3\chi M\lambda_s\left(1-\beta\Delta T-\frac{1}{2}\tanh\left(\frac{2\sigma}{\sigma_s}\right)\right)}{\dfrac{\mu_o M_s^2}{\left(\left(\frac{M_S^T}{3\chi H_{eff}}\right)^2-\operatorname{cosech}^2\left(\frac{3\chi H_{eff}}{M_S^T}\right)\right)} - 6\chi\sigma\lambda_s\left(1-\beta\Delta T-\frac{\sigma_s}{4\sigma}\ln\left(\cosh\left(\frac{2\sigma}{\sigma_s}\right)\right)\right)} \qquad (3)$$

where,

M is the magnetization of the magnetostrictive material,

M_S is the saturation magnetization at room temperature,

M_S^T is the saturation magnetization at a temperature T,

λ_S is the saturation magnetostrictive strain at room temperature,

H_{eff} is the effective applied magnetic field,

χ is the magnetic susceptibility of the magnetostrictive material,

σ is the compressive film stress,

σ_S is the stress at which magnetostrictive strain λ=λ_S [38],

ΔT is the change in temperature from a room temperature of 25°C,

β is the temperature coefficient of the magnetostrictive strain (λ), which is given by $\beta = -\frac{1}{\lambda}\frac{d\lambda}{dT}$,

γ is the temperature coefficient of the Young's modulus at magnetic saturation (E_S),

μ_0 is the vacuum permeability.

We implemented the static thermo-magneto-mechanical model for magnetostrictive materials through analytical and finite element simulations, separately. Analytically, we use the

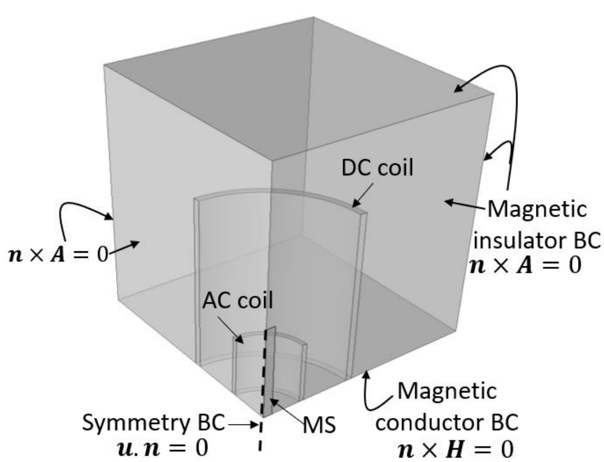

Figure 1: Computational domain of the finite element simulations. We model 1/8th of system utilizing the symmetry. MS – magnetostrictive sensor. The dimensions and relative positions of the coils and sensor correspond to our experimental setup which we discuss in Section III.

Supplementary Eqns. (S2)-(S4) to estimate the induced magnetization (M) using the applied magnetic field (H). Since the effective applied magnetic field (H_{eff}) is also coupled to the magnetization (M), we iterate the Supplementary Eqns. (S2)-(S4) to obtain the magnetization M for a given applied field H. We then use Eqns. (1)-(7) to predict the Young's modulus (E) and the resonance frequency (f_{res}) of the magnetostrictive sensor for different bias fields (H) and temperatures.

For finite element modeling, we use a computational domain shown in Figure 1. We model 1/8th of the system utilizing the symmetry in the computational domain. The boundary conditions are shown in Figure 1. A magnetic conductor ($\boldsymbol{n} \times \boldsymbol{H} = 0$, where $\boldsymbol{n}$ is the normal vector) boundary condition is applied to the bottom face of the domain, where the magnetic field is expected to be normal to the face. Magnetic insulator boundary condition ($\boldsymbol{n} \times \boldsymbol{A} = 0$) is applied to the remaining five faces of the domain where the magnetic field normal to the faces are expected to vanish. $\boldsymbol{A}$ is the magnetic vector potential. We applied symmetry boundary condition ($\boldsymbol{u}.\boldsymbol{n} = 0$, where $\boldsymbol{u}$ is the displacement vector) at the magnetostrictive sensor's two outer surfaces, which were cut to exploit the symmetry in the system. The dimensions of the coils and the sensor correspond to the experimental setup we used, which we discuss in Section III. We use COMSOL Multiphysics to solve Maxwell's equations and mechanical constitutive relations. We incorporated Eqns. (2)-(3) and Supplementary Eqns. (S1)-(S4) in the finite element model to capture the temperature and the magnetic field dependencies of the Young's modulus (E) of the magnetostrictive sensor. We then used eigenfrequency analysis to extract the resonance frequency (f_{res}) of the magnetostrictive sensor.

II. b. Lumped circuit model (dynamic analysis)

In the previous section, we discussed a static thermo-magneto-mechanical analysis to predict the material property variation with bias fields and temperatures. In this section, we model the vibrating magnetostrictive sensor using a lumped circuit model that couples the magnetic and kinematic circuits. Consider a magnetostrictive rod of area A and length l wrapped with a current-carrying coil (Figure 2). An ac current of I is supplied to the coil and the output voltage V is measured. We consider the kinematic circuit to be a parallel RLC network. Spring constant is modeled as an equivalent resistance (R), mass of the rod is modelled as an equivalent inductor (M), and compliance (C^H) is modelled as an equivalent capacitance. Compliance at a constant magnetic field is defined as $C^H = s^H\, l/A$, where s^H is the elastic compliance defined as $s^H = \frac{\partial \epsilon}{\partial \sigma}$ at a constant field H. We perform our analysis using the mobility representation of magnetostriction [39], where θ: 1 acts as the turns ratio of an electromechanical transformer relating the mechanical force F to the electric current I, and the velocity v to the voltage in the

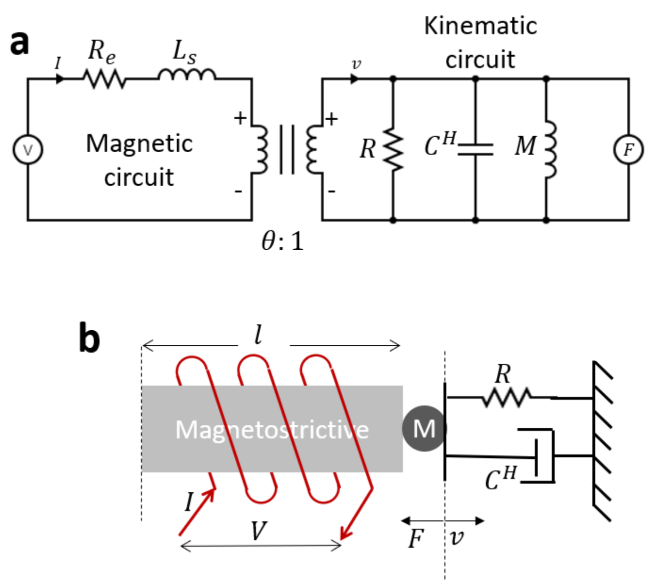

Figure 2: a) Equivalent circuit diagram of the electromechanical coupling between the ac coil and the magnetostrictive sensor. b) Schematic of the magnetostrictive material wrapped with a coil shown along with an equivalent free body diagram.

circuit, V.

The measured output voltage V in the magnetic circuit can be written as,

$$V = IR_e + j\omega L^S I + \frac{ANd}{s^H l} v \tag{4}$$

Where, R_e is the electrical resistance of the coil, L^S is the inductance of the coil, ω is the frequency of the ac current, N is the number of turns in the coil, v is the net velocity of the magnetostrictive rod's end surface, and d is the magnetostrictive constant defined as $d = \frac{\partial \epsilon}{\partial H}$ at a given stress. The net force in the magnetostrictive rod is given by,

$$F = \frac{-v}{\frac{1}{R} + j\omega C^H + \frac{1}{j\omega M}} + \frac{ANd}{s^H l} I \tag{5}$$

Since the magnetostrictive sensor is not constrained ($F = 0$), we can combine Eqns. (4) and (5), to get the measured output voltage V as,

$$V = IR_e + j\omega L^S I + \frac{\theta^2 R j\omega M I}{j\omega M + R(1 - \omega^2 C^H M)} \tag{6}$$

where, $\theta = \frac{ANd}{s^H l}$ is the electromechanical coupling factor. We can also represent the output voltage as $V = V_{ns} + V_{ind}$, where V_{ns} is the voltage across the coil when there is no magnetostrictive strip inside (corresponding to the first two terms in Eqn. (6)), and V_{ind} is the induced voltage due to the vibrating magnetostrictive strip (corresponding to the last term in Eqn. (6)).

III. Experimental setup

Figure 3 shows the schematic of the experimental setup to measure the magnetostrictive sensor response at different bath temperatures. We use Metglas 2605 TCA magnetostrictive strips (38 mm x 4 mm x 30 µm) taken from commercially available Sensormatic anti-theft tags. The Metglas strip is placed inside a sensing coil (ϕ17 mm x 25 mm) by vertically suspending the strip using a thread attached to the center. Keithley 6221 supplies the ac current to the sensing coil at a set frequency, whereas the Lock-in amplifier measures the ac voltage across the coil at the same frequency. In this configuration, the sensing coil is used to provide the actuation ac magnetic field, and also to simultaneously measure the induced emf due to the sensor. The sensing coil is placed inside a bias coil (ϕ40 mm x 70 mm), which provides the dc magnetic field. The coils and the sensor are placed inside a water beaker, which is attached with a flexible silicone heater to provide circumferential heating. The heater is controlled by a PID controller fitted with a thermocouple to control the temperature within the bath. Axial temperature variations across the heated water bath are typically less than 1 K at steady-state. We use a fluxgate magnetometer (TI DRV425EVM) to measure the magnetic field.

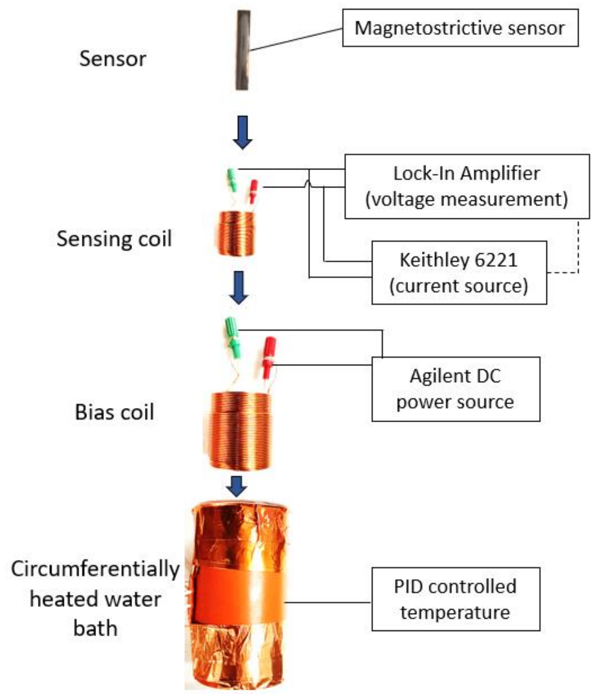

Figure 3: Schematic of the measurement setup used to measure the voltage response of magnetostrictive sensors at different bath temperatures.

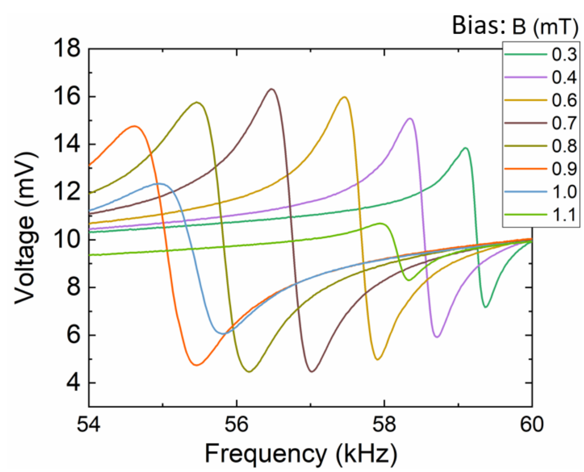

Figure 4: Voltage response of the ac coil housing the Metglas sensor in air at room temperature. The resonance frequency and the voltage amplitude at resonance are a function of the dc magnetic field (bias). An ac sensing current of 100 µA was used for actuation.

Figure 4 shows a typical voltage response of the magnetostrictive sensor in air at room temperature (25°C). We discuss the characteristics of the voltage response curve in detail in Section IV. Briefly, the voltage response during a frequency sweep shows a peak, followed by a trough near the resonance frequency. The resonance frequency and the voltage amplitude at resonance are a function of the dc magnetic field (bias) as shown in Figure 4. The resonance frequency and Q factor decrease with the bias field for fields <0.18 A, but they increase at higher bias magnetic fields (Supplementary Figure S2). On the other hand, the voltage amplitude initially increases with the bias field but decreases at higher bias magnetic fields (Figure 4). When the entire setup is placed in a water bath as shown in Figure 3, the Q factor of the sensor reduces, especially at very low and very high bias field (Supplementary Figures S1, S2). We changed the temperature of the water bath to observe the resonance frequency shifts with temperature as shown in Figure 5. We denote the resonance frequency at T_0=30°C as f_0. The shift in resonance frequency (Δf) due to temperature change is bias-dependent. At low bias fields, the resonance frequency decreases with temperature, whereas at high bias fields it increases with temperature. At intermediate and very high bias fields, the resonance frequency does not change significantly with temperature. We note that throughout this work, we extract the resonance frequency using the trough in the voltage response (Figure 4) for consistency, and that the analysis does not change

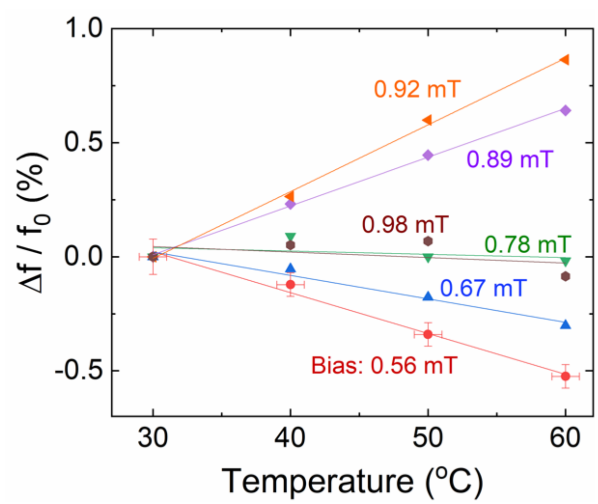

Figure 5: Shift in resonance frequency ($\Delta f/f_0$) in Metglas 2605 due to a temperature change in the water bath. f_0 corresponds to the resonance frequency at temperature T_0=30°C. The y-error bars correspond to 1σ fitting error in estimating the resonance frequency. The x-error bars correspond to the 1σ in temperatures measured in the heated water bath during measurement.

significantly if the peak is used instead. From the data in Figure 5 we find that the maximum TCF for the Metglas strip we used is ~0.03 %K^{-1} at 30°C.

IV. Results

We use our experimental results to first validate our models in Section IV.a. We use the static model to analyze the influence of different material properties on the TCF, in Section IV.b. Our dynamic model is then used to analyze the influence of the dimensions of the sensor in Section IV.c.

IV. a. Validation

Here, we validate our static and dynamic models with the experimental results. We plot the results of the thermo-magneto-mechanical (static) models in Figure 6. The experimental data points are shown as dots. The lines in Figure 6 are representative of the results from both the analytical calculations and finite element simulations. The results from the finite element simulations do not differ from that of the analytical model. We fit our model to our experimental data using

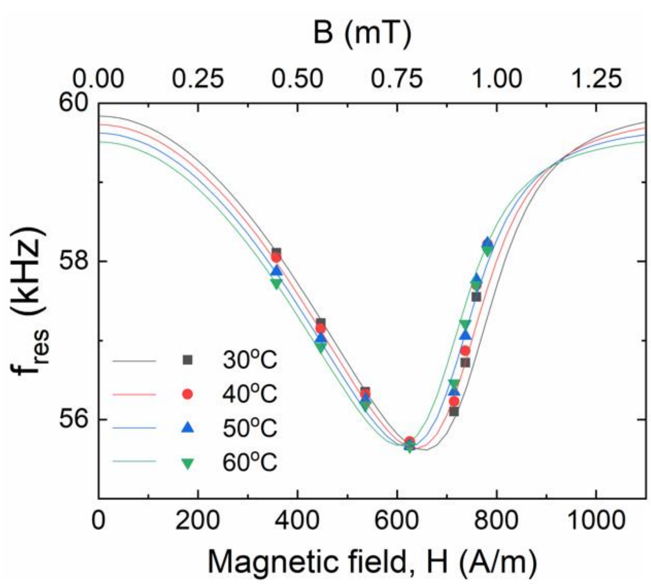

Figure 6: Resonance frequency of the Metglas 2605 strip at different temperatures and dc bias fields. The dots represent experimental data points. The solid lines are representative of the fitting from both the analytical model and finite element simulations separately. The fitting parameters are provided in the supplementary section.

$\gamma, \beta, \chi, \sigma, \sigma_S, E_S, M_S, \lambda_S$ as fitting parameters, where the initial values for some of the material properties ($\gamma, \beta, \chi, E_S, M_S, \lambda_S$) were taken from literature [40]–[48]. We provide the fitting parameters in the supplementary information. Small modifications within an order of magnitude to the literature values [40]–[48] resulted in a good fit to the experimental data as shown in Figure 6. At low bias magnetic fields, the resonance frequency is a strong function of the temperature. However, there is a cross-over in the temperature dependence of the resonance frequency at a bias field of ~0.75 mT. At the cross-over point (~0.75 mT), the resonance frequency is essentially temperature independent, as also evident from Figure 5. Similarly, there is a second cross-over at ~1.1 mT, where the resonance frequency is again temperature independent. In Section IV.b., we explain the significance and the reason behind these cross-over points. Overall, the thermo-magneto-mechanical model could qualitatively capture the experimentally observed resonance frequency variation with temperatures and bias fields.

We implemented the lumped circuit (dynamic) model analytically and used finite element simulations. First, we fit the analytical lumped circuit model (Eqn. (6)) to our experimental data as shown in Figure 7 using the terms in Eqn. (6) as fitting parameters. From Figure 7, we find that

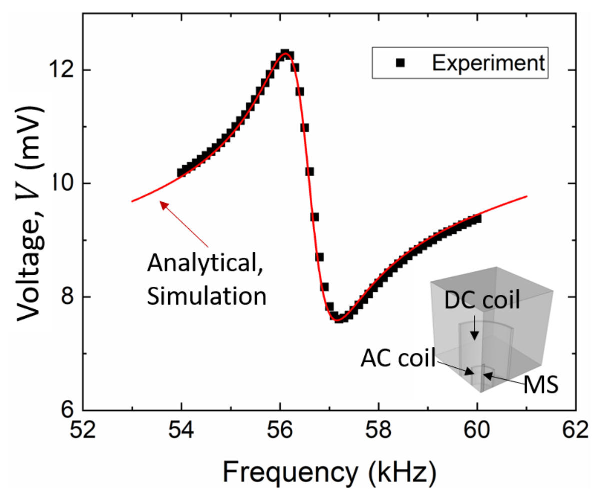

Figure 7: Voltage response of the ac coil housing the Metglas sensor in water at room temperature (25°C) at a dc bias field of 0.6 mT. Experimental data points are shown as black dots. The red solid line is representative of the results from both the analytical model and finite element simulations. The fitting parameters are provided in the supplementary section. Inset shows a schematic of the computational domain.

the analytical lumped circuit model could capture the voltage response of the magnetostrictive sensor during a frequency sweep. We then use the analytically estimated fit parameters R_e and L^S for the V_{ns} term in the finite element model. For the finite element model, we model the output voltage as $V = V_{ns} + \Theta V_{ind}$, where $V_{ns} = IR_e + j\omega L^S I$ uses the analytically estimated fit parameters R_e and L^S; induced voltage V_{ind} due to the magnetostrictive sensor is obtained from the Maxwell solver as $V = \oint E.dl$ across the coil, and Θ is the fitting parameter. We use a frequency domain solver to estimate the induced voltage for a range of frequencies. The Young's modulus of the material was estimated for the applied dc field using the static thermo-magneto-mechanical model described in Section II. a. The red line in Figure 7 is representative of the fitting from both the analytical lumped circuit model and that of the finite element simulation. We provide details on the fitting parameters in the supplementary section. Overall, both the lumped circuit model and the finite element simulations can capture the coupling between the magnetic and kinematic circuits.

IV. b. Material properties influencing TCF

We use the validated thermo-magneto-mechanical model (Eqns. (2)-(3)) to find the material properties that influence the temperature coefficient of resonance frequency (TCF). The resonance frequency is a function of the length of the sensor (L) and the Young's modulus (E), both of which vary with the temperature. The thermal expansion coefficient (α), defined as $\alpha = \frac{1}{L}\frac{dL}{dT}$ is typically small, in the order of 10^{-6} K^{-1}, and hence does not contribute significantly to the change in the resonance frequency when $\Delta T \sim 10$ K. The temperature dependence of the Young's modulus is therefore more dominant in causing a change in the resonance frequency. We define the temperature coefficient of Young's modulus as $TCE = \frac{1}{E}\frac{\partial E}{\partial T}$. The magnitude of the temperature coefficient of resonance frequency (TCF) is then directly proportional to TCE. As evident from Eqns. (2)-(3), E is a function of several material properties such as $\gamma, \beta, \chi, \sigma, M_S$, etc. in addition to the applied field (H) and temperature (T). To analyze the temperature dependence of E with respect to these material properties, we look at three regimes: (1) low applied magnetic field, when $M \to 0$, (2) high applied magnetic field, when $M \sim M_S/2$, and (3) at saturation magnetic fields, when $M \to M_s$.

At low magnetic fields, when $M \to 0$, the temperature coefficient of Young's modulus can be approximated as $TCE = \frac{1}{E}\frac{\partial E}{\partial T} = \gamma$ from Eqn. (2). Even though γ is the temperature coefficient of Young's modulus at magnetic saturation (E_S), γ directly influences the temperature coefficient of Young's modulus (TCE) and hence TCF even at low magnetic fields (when $M \rightarrow 0$).

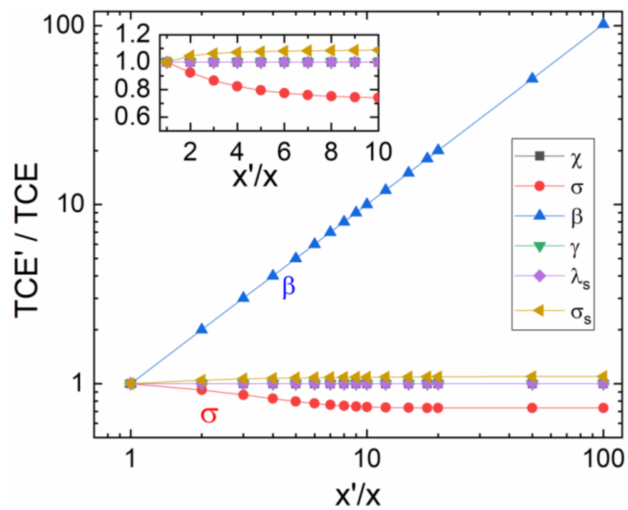

Figure 8: The change in temperature coefficient of Young's modulus (TCE) is plotted against the change in various material parameters at high magnetic fields (when $M{\sim}M_S/2$). x corresponds to one of the material and fitting parameters: $\chi, \sigma, \beta, \gamma, \lambda_s, \sigma_S$. Initial values for x were: χ=1, γ=10^{-4} K^{-1}, β= 10^{-4} K^{-1}, λ_S=10^{-6}, σ_S=10 MPa, σ=1 MPa. The inset shows the variation in TCE'/TCE for material parameters other than β.

At high magnetic fields, when $M{\sim}M_S/2$, the temperature coefficient of Young's modulus can be written as,

$$TCE = \left(\frac{1}{E}\frac{\partial E}{\partial T}\right)_{M\sim M_S/2} \sim -\frac{\partial\left(\frac{\partial M}{\partial \sigma}\right)}{\partial T}\frac{1}{\left(\frac{\partial M}{\partial \sigma}\right)^2}\left(\frac{\partial M}{\partial \sigma}\right)_{\Delta T=0} \quad (7)$$

For a change in a given material property from x (say) to x', we plot in Figure 8, the change in the corresponding temperature coefficient of Young's modulus from TCE to TCE', when the other material properties are kept constant. Here, x represents one of the material properties: $\chi, \sigma, \beta, \gamma, \lambda_S$. We find from Figure 8 that the temperature coefficient of magnetostriction, β, dominates the other properties in influencing the temperature coefficient of Young's modulus. The inset in Figure 8 shows that the compressive film stress σ could reduce the temperature coefficient of Young's modulus by up to ~20%. Other material properties or fitting parameters do not influence the temperature sensitivity significantly (<10%) at high magnetic fields. Therefore, at high magnetic fields (when $M \sim M_S/2$), the temperature coefficient of magnetostriction strain, β, directly influences the temperature coefficient of resonance frequency (TCF), whereas the film stress, σ, negatively influences the TCF.

At saturation magnetic fields (when $M \rightarrow M_S$), the temperature coefficient of Young's modulus is given by $TCE = \frac{1}{E}\frac{\partial E}{\partial T} = \gamma$ from Eqn. (2), which is similar to regime 1 (when $M \rightarrow 0$) for low applied magnetic fields. We discussed three different regimes, and they can be observed in Figure 6 from the two cross-over points because γ and β have opposite signs in Metglas (see Supplementary Information). The temperature coefficient of resonance frequency (TCF) for bias fields from 0 mT to ~0.75 mT is governed by γ; TCF for bias fields from ~0.75 mT to ~1.1 mT is governed primarily by β; and TCF for bias fields ≫ 1.1 mT is governed by γ. We discuss in Section V how we can use these material properties to identify magnetostrictive materials that could have higher TCF.

IV. c. Length-scale dependence of induced voltage

In this Section, we study the influence of the dimensions of the magnetostrictive sensor on the induced voltage in the coil. This could be useful in determining the minimum size of the sensor that can be used, and the number of sensors required. We use the validated finite element model that captured electromechanical coupling (in Figure 7). Using the same configuration of coils that we used in our experimental setup and the finite element simulations, we change the dimensions of the magnetostrictive sensor and observe the change in the peak induced voltage (denoted by V_{ind}^P) using simulations. We used the same Rayleigh damping coefficients for all the simulations. In Figure 9, we plot the ratio of V_{ind}^P over V_{ns}, which is representative of the signal-to-background ratio, for different lengths l and widths w_r of the sensor. The no-strip voltage, V_{ns}, is the baseline voltage that is present even without a magnetostrictive sensor. From Figure 9, we find that the signal-to-background ratio (V_{ind}^P/V_{ns}) reaches zero when the length of the magnetostrictive sensor is ~10 mm. Similarly, the signal (V_{ind}^P) drops roughly by half when the width w_r of the sensor is reduced by half. Therefore, for the current configuration of measurement (Figure 3, Figure 1), we expect the signal-to-background ratio to vary linearly with the length and width of the sensor, especially when l:10-40 mm, w_r:2-4 mm.

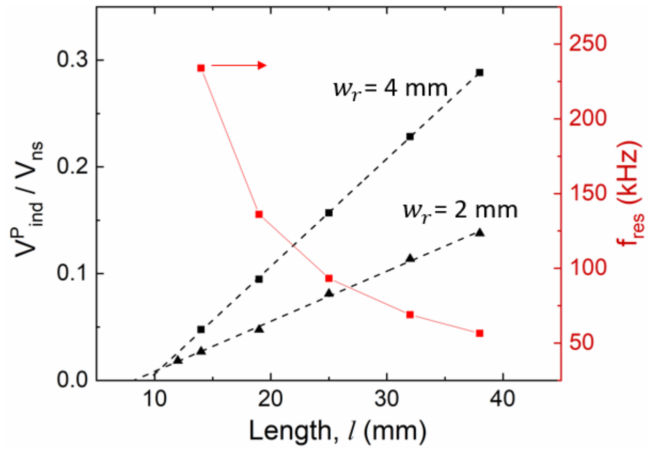

Figure 9: Signal-to-background ratio at the ac coil for different Metglas sensor dimensions are plotted along the left y-axis. The data points shown in dots are from simulations. The dashed lines are straight line fits to the simulated data. The solid red line connects the corresponding data points. The coil dimensions correspond to that of the experimental setup described in Section III.

The signal-to-background ratio (V_{ind}^{P}/V_{ns}) drops to zero (in Figure 9) primarily because the background (V_{ns}) increases at high frequencies. The background signal is given by $V_{ns} = IR_e + j\omega L^S I$, where, $j\omega L^S$, the self-inductance component, is directly proportional to the frequency of operation, ω. When the sensor length l is reduced, the resonance frequency increases as shown in Figure 9, which in turn increases the background signal (V_{ns}), obscuring the signal-to-background ratio. The background signal (V_{ns}) increases 4-fold from 9.5 mV to 38 mV (Figure 10), when the sensor length is decreased from 38 mm to 14 mm. On the other hand, the peak induced voltage (V_{ind}^{P}) decreases ~2-fold from 2.8 mV to 1.8 mV. Therefore, when using a small sensor, the reduction in the signal-to-background (V_{ind}^{P}/V_{ns}) ratio is primarily due to the self-inductance of the ac coil at high frequencies.

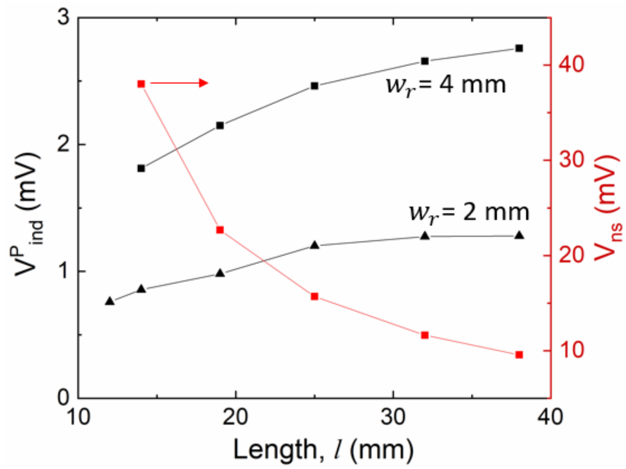

Figure 10: The peak induced voltage (V_{ind}^{P}) at the ac coil is plotted for different Metglas sensor dimensions on the left y-axis. The voltage at the ac coil with no magnetostrictive strip (V_{ns}) is shown on the right y-axis. The data points shown in dots are from simulations. The solid lines connect the shown data points. The coil dimensions correspond to that of the experimental setup, which is discussed in Section III.

V. Discussion

In this work, we first experimentally measured the shift in the resonance frequency of a magnetostrictive sensor due to temperature changes. We then analytically and computationally analyzed the material properties responsible for the shift in resonance frequency due to temperature changes. We also analyzed the influence of the sensor size on the overall measurement. In this section, we extend our analysis and provide ways to improve the sensitivity to temperature changes. We also discuss potential applications and limitations.

In Section IV.b., our sensitivity analysis revealed that the temperature coefficient of resonance frequency (TCF) is directly dependent on (1) γ – temperature coefficient of E_S, at low ($M \rightarrow 0$) and saturation ($M \rightarrow M_S$) bias magnetic fields, and (2) β – temperature coefficient of magnetostriction strain (λ), at high bias magnetic fields (when $M \sim M_S/2$). From the analytical fitting in Figure 6, we determined γ for the Metglas sensor to be 3.6×10^{-4} K^{-1}. Among other magnetostrictive materials, Terfenol was previously reported [32] to have a higher $\gamma\sim$ 4.2×10^{-3} K^{-1}. We repeated our experiments using Terfenol (Figure 11) and found the temperature coefficient of resonance frequency (TCF) to be ~0.14% K^{-1}, which is almost 5-fold higher than that of the Metglas sensor (~0.03% K^{-1}) for a $\Delta T \sim 10$ K. Even though the coefficient of magnetostriction (β) for Terfenol is comparable to that of Metglas, a higher γ potentially resulted in a higher TCF for Terfenol. Further, our thermo-magneto-mechanical model could capture the resonance frequency shifts in Terfenol as shown in Supplementary Figure S4. We note that a previous work [29] on $Fe_{40}Ni_{40}B_{20}$ alloy reported a TCF~0.15% K^{-1}, which is comparable to the TCF we report for Terfenol. The TCF from $Fe_{40}Ni_{40}B_{20}$ is higher than the Metglas sensor we report, possibly because of a higher β, which is also evident from a wider spread in their resonance frequencies at higher magnetic fields [29]. Even though Terfenol has a higher TCF (~0.14% K^{-1}), the susceptibility $\chi \sim 80$ is much lower than that of Metglas ($\chi \sim 50{,}000$). Thus, Terfenol requires higher bias magnetic fields (~5-10 mT) than that required for Metglas (~0.2-0.6 mT). Future work can focus on identifying materials with a high susceptibility (χ) that also have high γ and/or β to have a higher temperature coefficient of resonance frequency (TCF) at low bias fields (<1 mT).

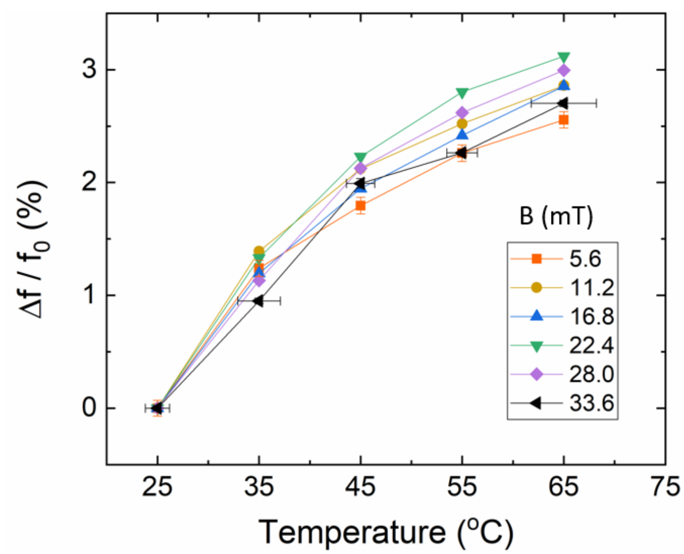

Figure 11: Shift in the resonance frequency ($\Delta f/f_0$) in a Terfenol transducer (53 mm × 17 mm × 1.2 mm) due to a temperature change in the water bath. f_0 corresponds to the resonance frequency at temperature T_0=25°C.

Throughout this work, we focused on the shift in resonance frequency as a potential sensing parameter to measure temperatures. However, an alternative temperature sensing technique can be developed by measuring the voltage across the ac coil at a fixed frequency near the resonance frequency of the magnetostrictive sensor. We explain it using a Metglas sensor in the same experimental setup (Figure 3). In Figure 12a, we plot the ratio $\Delta V/V_0$, where V_0 is the voltage measured at 30°C and ΔV corresponds to the difference in the measured ac voltage amplitude between 60°C and 30°C bath temperatures. The magnitude of $\Delta V/V_0$ reaches a maximum at 55.7 kHz, at a bias field of 0.89 mT. At this frequency (55.7 kHz) and bias field (0.89 mT), we plot the $\Delta V/V_0$ in the inset (Figure 12b). We find that the $\Delta V/V_0$ directly increases with temperature. If we define a temperature coefficient of the measured ac voltage as $TCV = \frac{\Delta V}{V_0}\frac{1}{\Delta T}$, the TCV is roughly 0.8% K^{-1}. The TCV can be maximized by choosing a frequency and a bias field where the magnitude of $\Delta V/V_0$ is the highest across the temperature range desired (Figure 12). Measuring the TCF can be time consuming and require sophisticated equipment such as network analyzers, whereas TCV can be easily measured using digital multimeters or lock-in amplifiers. The TCV can be used for temperature sensing only when the frequency shift (Δf) due to a temperature change (ΔT) is less than the width of the resonance curve. In other words, the Q-

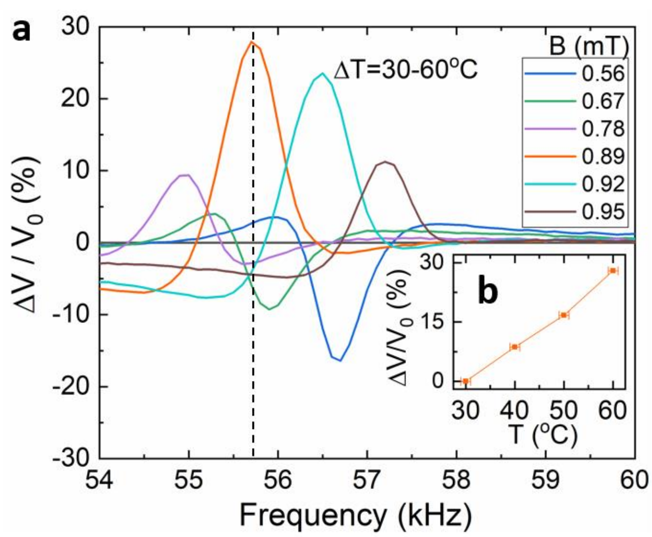

Figure 12: a) Shift in the voltage ($\Delta V/V_0$) at the ac coil due to a change in the temperature of the water bath plotted for different bias fields over a range of frequencies. ΔV corresponds to the change in the measured voltage due to a temperature change from 30°C to 60°C. V_0 is the measured voltage at 30°C. A Metglas sensor was used in setup similar to Figure 3. b) Inset plots the voltage shifts for different temperatures at a frequency of 55.7 kHz and a bias field of 0.89 mT.

factor of the sensor must be smaller than $(TCF.\Delta T)^{-1}$. For the Metglas sensor, the Q-factor in water is ~30, whereas $(TCF.\Delta T)^{-1}$ is ~ 110 for a ΔT= 30°C, thus allowing us to use TCV for temperature sensing. Further, the TCV could be a function of the position and orientation of the sensor with respect to the ac sensing/transmit coil. Therefore, the temperature coefficient of the voltage (TCV) of the ac coil can be used for temperature sensing, especially in places where the relative position and orientation of the magnetostrictive sensor remains constant with respect to the coil.

In this work, we used a concentric coil configuration to serve as proof-of-concept experiments. Helmholtz coils and/or permanent magnets can also be used instead. For instance, the bias coil can be replaced by a ferromagnet magnetized to provide the appropriate bias field. The magnetostrictive sensor strip can be packaged along with the ferromagnet in a manner similar to the commercially available anti-theft tags [16]. Further, the commercially available anti-theft tags can also be repurposed to measure temperatures either using the TCF- or TCV-based method. We discussed in Section IV.c. that the signal-to-background ratio (V_{ind}^{P}/V_{ns}) drops when the sensor dimensions are reduced. This can be overcome by two possible methods. First, two separate transmit and receive coils can be placed perpendicular to each other to decouple them and remove any self-inductance effects [48]. Second, multiple thin-film magnetostrictive sensors can be packaged together to increase the signal-to-background ratio [49]. A magnetostrictive temperature sensor package can enable *in situ* near-field applications. For instance, they can potentially enable long-term near-field temperature measurements in food packaging [17], [36], culture medium [50]–[52], implantable biomedical devices [4], [53], etc., and for concurrent temperature and fouling measurements in industrial pipelines [34], especially in low-temperature heat exchangers [54]–[56] to ensure profitable heat recovery. Overall, new or existing magnetostrictive sensor packages can be suitably adapted to measure temperatures remotely, using either the TCF- or TCV-based technique.

VI. Conclusion

In summary, we modeled and analyzed magnetostrictive materials for use in potential wireless temperature sensing systems. We first experimentally measured the temperature coefficient of resonance frequency (TCF) in a Metglas 2605 TCA strip to be ~0.03%K^{-1}. We then implemented thermo-magneto-mechanical constitutive equations using both analytical and finite element methods to model the magnetostriction-based sensing system. The analytical and computational models developed in this work provide a general framework for the sensitivity analysis of magnetostriction-based temperature sensing, and can be suitably adapted to any configuration of the sensing scheme. Through our sensitivity analysis, we identified the material properties of interest and demonstrated a 5-fold improvement to the TCF by using Terfenol. We also explored an alternate temperature sensing scheme that reduces instrument complexity by using the temperature coefficient of ac voltage (TCV) at the coil, which could be used if the sensor and coil locations are fixed relative to each other. In contrast to RFID- or SAW-based sensors, magnetostrictive transducers offer a simple and passive near-field temperature sensing technique. From a broader perspective, this work provides ways to use new or repurposed existing magnetostrictive sensor packages to enable remote temperature measurements.

Acknowledgment:

This work was supported in part by funding from the National Science Foundation through Grant No. NSF-CBET-17-06854

Supplementary Information:

See supplementary information for additional details on the thermo-magneto-mechanical model, more validation cases, and fitting parameters for Figures 6,7.

Data availability:

The data that support the findings of this study are available from the corresponding author upon reasonable request.

References

[1] Narrijun Cho, Seong-Jun Song, Jae-Youl Lee, Sunyoung Kim, Shiho Kim, and Hoi-Jun Yoo, "A 8-/spl mu/W, 0.3-mm/sup 2/ RF-powered transponder with temperature sensor for wireless environmental monitoring," in *2005 IEEE International Symposium on Circuits and Systems*, May 2005, pp. 4763-4766 Vol. 5, doi: 10.1109/ISCAS.2005.1465697.

[2] "RFM3200 Wireless Flexible Temperature Sensor," *Axzon website*. https://axzon.com/rfm3200-wireless-flexible-temperature-sensor/ (accessed Oct. 26, 2020).

[3] S. Saha and A. Majumdar, "Data centre temperature monitoring with ESP8266 based Wireless Sensor Network and cloud based dashboard with real time alert system," in *2017 Devices for Integrated Circuit (DevIC)*, Mar. 2017, pp. 307–310, doi: 10.1109/DEVIC.2017.8073958.

[4] "CorTemp Sensor," *HQ, Inc.* https://hqinc.net/home/cortemp/cortemp-products/cortemp-sensor/ (accessed Aug. 21, 2020).

[5] D. Girbau, Á. Ramos, A. Lazaro, S. Rima, and R. Villarino, "Passive Wireless Temperature Sensor Based on Time-Coded UWB Chipless RFID Tags," *IEEE Transactions on Microwave Theory and Techniques*, vol. 60, no. 11, pp. 3623–3632, Nov. 2012, doi: 10.1109/TMTT.2012.2213838.

[6] K. Opasjumruskit *et al.*, "Self-powered wireless temperature sensors exploit RFID technology," *IEEE Pervasive Computing*, vol. 5, no. 1, pp. 54–61, Jan. 2006, doi: 10.1109/MPRV.2006.15.

[7] K. G. Ong, C. A. Grimes, C. L. Robbins, and R. S. Singh, "Design and application of a wireless, passive, resonant-circuit environmental monitoring sensor," *Sensors and Actuators A: Physical*, vol. 93, no. 1, pp. 33–43, Aug. 2001, doi: 10.1016/S0924-4247(01)00624-0.

[8] Y. Wang, Y. Jia, Q. Chen, and Y. Wang, "A Passive Wireless Temperature Sensor for Harsh Environment Applications," *Sensors*, vol. 8, no. 12, Art. no. 12, Dec. 2008, doi: 10.3390/s8127982.

[9] V. Kalinin, "Passive wireless strain and temperature sensors based on SAW devices," in *Proceedings. 2004 IEEE Radio and Wireless Conference (IEEE Cat. No.04TH8746)*, Sep. 2004, pp. 187–190, doi: 10.1109/RAWCON.2004.1389104.

[10] L. Reindl, G. Scholl, T. Ostertag, C. C. W. Ruppel, W.- Bulst, and F. Seifert, "SAW devices as wireless passive sensors," in *1996 IEEE Ultrasonics Symposium. Proceedings*, Nov. 1996, vol. 1, pp. 363–367 vol.1, doi: 10.1109/ULTSYM.1996.583993.

[11] G. A. Borrero, J. P. Bravo, S. F. Mora, S. Velásquez, and F. E. Segura-Quijano, "Design and fabrication of SAW pressure, temperature and impedance sensors using novel multiphysics simulation models," *Sensors and Actuators A: Physical*, vol. 203, pp. 204–214, Dec. 2013, doi: 10.1016/j.sna.2013.08.021.

[12] M. Gallagher, "Design, Fabrication, and Interrogation of Integrated Wireless SAW Temperature Sensors," 2015.

[13] K. Mc Gee, P. Anandarajah, and D. Collins, "A Review of Chipless Remote Sensing Solutions Based on RFID Technology," *Sensors*, vol. 19, no. 22, Art. no. 22, Jan. 2019, doi: 10.3390/s19224829.

[14] R. R. Fletcher, "Low-cost electromagnetic tagging : design and implementation," Thesis, Massachusetts Institute of Technology, 2002.

[15] E. Langlois *et al.*, “Magnetic Smart Tags (MaST) for Arms Control and Treaty Verification.,” Sandia National Lab. (SNL-NM), Albuquerque, NM (United States), SAND2016-9417, Sep. 2016. doi: 10.2172/1562661.
[16] G. Herzer, “Magnetic materials for electronic article surveillance,” *Journal of Magnetism and Magnetic Materials*, vol. 254–255, pp. 598–602, Jan. 2003, doi: 10.1016/S0304-8853(02)00930-7.
[17] S. Li, A. Simonian, and B. A. Chin, “Sensors for Agriculture and the Food Industry,” *Electrochem. Soc. Interface*, vol. 19, no. 4, p. 41, Jan. 2010, doi: 10.1149/2.F05104if.
[18] C. A. Grimes and D. Kouzoudis, “Remote query measurement of pressure, fluid-flow velocity, and humidity using magnetoelastic thick-film sensors,” *Sensors and Actuators A: Physical*, vol. 84, no. 3, pp. 205–212, Sep. 2000, doi: 10.1016/S0924-4247(00)00306-X.
[19] D. Kouzoudis and C. A. Grimes, “The frequency response of magnetoelastic sensors to stress and atmospheric pressure,” *Smart Mater. Struct.*, vol. 9, no. 6, pp. 885–889, Nov. 2000, doi: 10.1088/0964-1726/9/6/320.
[20] D. Kouzoudis and C. A. Grimes, “Remote query fluid-flow velocity measurement using magnetoelastic thick-film sensors (invited),” *Journal of Applied Physics*, vol. 87, no. 9, pp. 6301–6303, Apr. 2000, doi: 10.1063/1.372686.
[21] C. A. Grimes, D. Kouzoudis, and C. Mungle, “Simultaneous measurement of liquid density and viscosity using remote query magnetoelastic sensors,” *Review of Scientific Instruments*, vol. 71, no. 10, pp. 3822–3824, Sep. 2000, doi: 10.1063/1.1315352.
[22] K. T. Loiselle and C. A. Grimes, “Viscosity measurements of viscous liquids using magnetoelastic thick-film sensors,” *Review of Scientific Instruments*, vol. 71, no. 3, pp. 1441–1446, Mar. 2000, doi: 10.1063/1.1150477.
[23] M. K. Jain, S. Schmidt, K. G. Ong, C. Mungle, and C. A. Grimes, “Magnetoacoustic remote query temperature and humidity sensors,” *Smart Mater. Struct.*, vol. 9, no. 4, pp. 502–510, Aug. 2000, doi: 10.1088/0964-1726/9/4/314.
[24] Y. Yamamoto, T. Makino, and H. Matsui, “Micro-positioning and actuation devices using giant magnetostriction materials,” in *Proceedings 2000 ICRA. Millennium Conference. IEEE International Conference on Robotics and Automation. Symposia Proceedings (Cat. No.00CH37065)*, Apr. 2000, vol. 4, pp. 3635–3640 vol.4, doi: 10.1109/ROBOT.2000.845298.
[25] M. J. Dapino, “On magnetostrictive materials and their use in adaptive structures,” *Structural Engineering and Mechanics*, vol. 17, no. 3_4, pp. 303–329, 2004, doi: 10.12989/sem.2004.17.3_4.303.
[26] F. Claeyssen, N. Lhermet, R. Le Letty, and P. Bouchilloux, “Actuators, transducers and motors based on giant magnetostrictive materials,” *Journal of Alloys and Compounds*, vol. 258, no. 1, pp. 61–73, Aug. 1997, doi: 10.1016/S0925-8388(97)00070-4.
[27] C. A. Grimes *et al.*, “Wireless Magnetoelastic Resonance Sensors: A Critical Review,” *Sensors*, vol. 2, no. 7, Art. no. 7, Jul. 2002, doi: 10.3390/s20700294.
[28] M. K. Jain and C. A. Grimes, “A wireless magnetoelastic micro-sensor array for simultaneous measurement of temperature and pressure,” *IEEE Transactions on Magnetics*, vol. 37, no. 4, pp. 2022–2024, Jul. 2001, doi: 10.1109/20.951041.
[29] A. García-Arribas, D. De Cos, J. Gutiérrez, and J. M. Barandiarán, “Selectable temperature sensitivity of the magnetoelastic resonance,” *Sensors and Actuators A: Physical*, vol. 106, no. 1, pp. 111–116, Sep. 2003, doi: 10.1016/S0924-4247(03)00146-8.

[30] X. J. Zheng and L. Sun, “A nonlinear constitutive model of magneto-thermo-mechanical coupling for giant magnetostrictive materials,” *Journal of Applied Physics*, vol. 100, no. 6, p. 063906, Sep. 2006, doi: 10.1063/1.2338834.

[31] K. Jin, Y. Kou, and X. Zheng, “A nonlinear magneto-thermo-elastic coupled hysteretic constitutive model for magnetostrictive alloys,” *Journal of Magnetism and Magnetic Materials*, vol. 324, no. 12, pp. 1954–1961, Jun. 2012, doi: 10.1016/j.jmmm.2012.01.028.

[32] Y. Liang and X. Zheng, “Experimental researches on magneto-thermo-mechanical characterization of Terfenol-D,” *Acta Mechanica Solida Sinica*, vol. 20, no. 4, pp. 283–288, Dec. 2007, doi: 10.1007/s10338-007-0733-x.

[33] Y. Xiao, H.-M. Zhou, and X.-L. Cui, “Nonlinear resonant magnetoelectric coupling effect with thermal, stress and magnetic loadings in laminated composites,” *Composite Structures*, vol. 128, pp. 35–41, Sep. 2015, doi: 10.1016/j.compstruct.2015.03.039.

[34] S. Vinogradov and J. L. Fisher, “New Magnetostrictive Transducers and Applications for SHM of Pipes and Vessels,” presented at the ASME 2019 Pressure Vessels & Piping Conference, Nov. 2019, doi: 10.1115/PVP2019-94078.

[35] M. Wiercigroch, V. Vaziri, and M. Kapitaniak, “RED: Revolutionary Drilling Technology for Hard Rock Formations,” presented at the SPE/IADC Drilling Conference and Exhibition, Mar. 2017, doi: 10.2118/184665-MS.

[36] A. L. Brody, “State of the art of active/intelligent food packaging,” *Institute of Food Technologists Food Packaging Summit*, 2006.

[37] C. Liang, S. Morshed, and B. C. Prorok, “Correction for longitudinal mode vibration in thin slender beams,” *Appl. Phys. Lett.*, vol. 90, no. 22, p. 221912, May 2007, doi: 10.1063/1.2745262.

[38] “A nonlinear constitutive model for Terfenol-D rods: Journal of Applied Physics: Vol 97, No 5,” Accessed: Aug. 20, 2020. [Online]. Available: https://aip.scitation.org/doi/10.1063/1.1850618.

[39] G. Engdahl, *Handbook of Giant Magnetostrictive Materials*. Elsevier, 2000.

[40] A. P. Thomas and M. R. J. Gibbs, “Anisotropy and magnetostriction in metallic glasses,” *Journal of Magnetism and Magnetic Materials*, vol. 103, no. 1, pp. 97–110, Jan. 1992, doi: 10.1016/0304-8853(92)90242-G.

[41] “Materials from Metglas®, Inc.,” *Metglas, Inc.* https://metglas.com/magnetic-materials/ (accessed Aug. 21, 2020).

[42] R. Schulz, N. Alexandrov, J. Tétreault, R. Simoneau, and R. Roberge, “Development and application of amorphous core-distribution transformers in Québec,” *JMEP*, vol. 4, no. 4, pp. 430–434, Aug. 1995, doi: 10.1007/BF02649303.

[43] G. H. Hayes, W. A. Hines, D. P. Yang, and J. I. Budnick, “Low field magnetic anisotropy in Metglas 2605 CO ribbons,” *Journal of Applied Physics*, vol. 57, no. 8, pp. 3511–3513, Apr. 1985, doi: 10.1063/1.335044.

[44] J. Zhai, S. Dong, Z. Xing, J. Li, and D. Viehland, “Giant magnetoelectric effect in Metglas/polyvinylidene-fluoride laminates,” *Appl. Phys. Lett.*, vol. 89, no. 8, p. 083507, Aug. 2006, doi: 10.1063/1.2337996.

[45] M. H. Kim, K. S. Lee, and S. H. Lim, “Magnetostriction measurements of metallic glass ribbon by fiber-optic Mach–Zehnder interferometry,” *Journal of Magnetism and Magnetic Materials*, vol. 191, no. 1, pp. 107–112, Jan. 1999, doi: 10.1016/S0304-8853(98)00310-2.

[46] B. Kundys, Y. Bukhantsev, H. Szymczak, M. R. J. Gibbs, and R. Zuberek, “Temperature dependence of saturation magnetostriction measured for Fe81Si3.5B13.5C2 amorphous

films by a bending method based on the Villari effect," *J. Phys. D: Appl. Phys.*, vol. 35, no. 11, pp. 1095–1098, May 2002, doi: 10.1088/0022-3727/35/11/301.
[47] Z. Turgut, H. Kosai, T. Bixel, J. Scofield, S. L. Semiatin, and J. Horwath, "Hysteresis loss analysis of soft magnetic materials under direct current bias conditions," *Journal of Applied Physics*, vol. 117, no. 17, p. 17A508, May 2015, doi: 10.1063/1.4919228.
[48] S. R. Green and Y. B. Gianchandani, "Wireless Magnetoelastic Monitoring of Biliary Stents," *Journal of Microelectromechanical Systems*, vol. 18, no. 1, pp. 64–78, Feb. 2009, doi: 10.1109/JMEMS.2008.2008568.
[49] J. Tang, S. R. Green, and Y. B. Gianchandani, "Scalable, high-performance magnetoelastic tags using frame-suspended hexagonal resonators," *J. Micromech. Microeng.*, vol. 24, no. 6, p. 065006, Apr. 2014, doi: 10.1088/0960-1317/24/6/065006.
[50] S. Hur, R. Mittapally, S. Yadlapalli, P. Reddy, and E. Meyhofer, "Sub-nanowatt resolution direct calorimetry for probing real-time metabolic activity of individual C. elegans worms," *Nature Communications*, vol. 11, no. 1, Art. no. 1, Jun. 2020, doi: 10.1038/s41467-020-16690-y.
[51] M. C. Rajagopal *et al.*, "Transient heat release during induced mitochondrial proton uncoupling," *Communications Biology*, vol. 2, no. 1, Art. no. 1, Jul. 2019, doi: 10.1038/s42003-019-0535-y.
[52] S. Hong *et al.*, "Sub-nanowatt microfluidic single-cell calorimetry," *Nature Communications*, vol. 11, no. 1, Art. no. 1, Jun. 2020, doi: 10.1038/s41467-020-16697-5.
[53] R. Lin *et al.*, "Wireless battery-free body sensor networks using near-field-enabled clothing," *Nature Communications*, vol. 11, no. 1, Art. no. 1, Jan. 2020, doi: 10.1038/s41467-020-14311-2.
[54] M. C. Rajagopal *et al.*, "Materials-to-device design of hybrid metal-polymer heat exchanger tubes for low temperature waste heat recovery," *International Journal of Heat and Mass Transfer*, vol. 143, p. 118497, Nov. 2019, doi: 10.1016/j.ijheatmasstransfer.2019.118497.
[55] X. Chen, Y. Su, D. Reay, and S. Riffat, "Recent research developments in polymer heat exchangers – A review," *Renewable and Sustainable Energy Reviews*, vol. 60, pp. 1367–1386, Jul. 2016, doi: 10.1016/j.rser.2016.03.024.
[56] S. Sundar *et al.*, "Fouling modeling and prediction approach for heat exchangers using deep learning," *International Journal of Heat and Mass Transfer*, vol. 159, p. 120112, Oct. 2020, doi: 10.1016/j.ijheatmasstransfer.2020.120112.

Supplementary information

Design and analysis of magnetostrictive sensors for wireless temperature sensing

Manjunath C. Rajagopal and Sanjiv Sinha*

Department of Mechanical Science and Engineering

University of Illinois at Urbana-Champaign, Urbana, IL 61801, USA

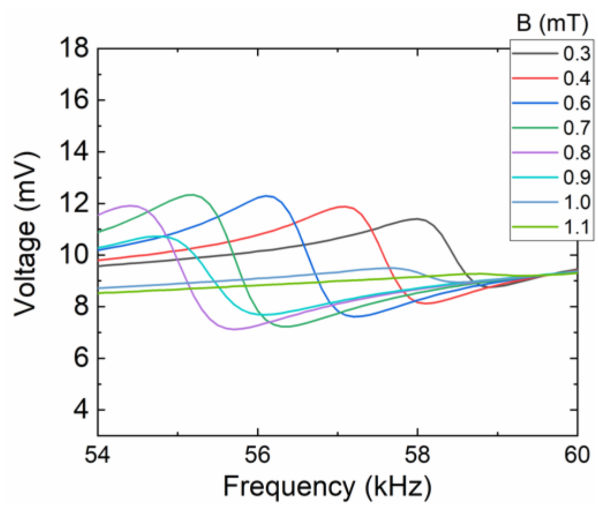

Figure S1. The voltage response of the Metglas 2605 TCA sensor in water at room temperature. The resonance frequency and the voltage amplitude at resonance are a function of the dc magnetic field (bias). An ac sensing current of 100 μA was used for actuation.

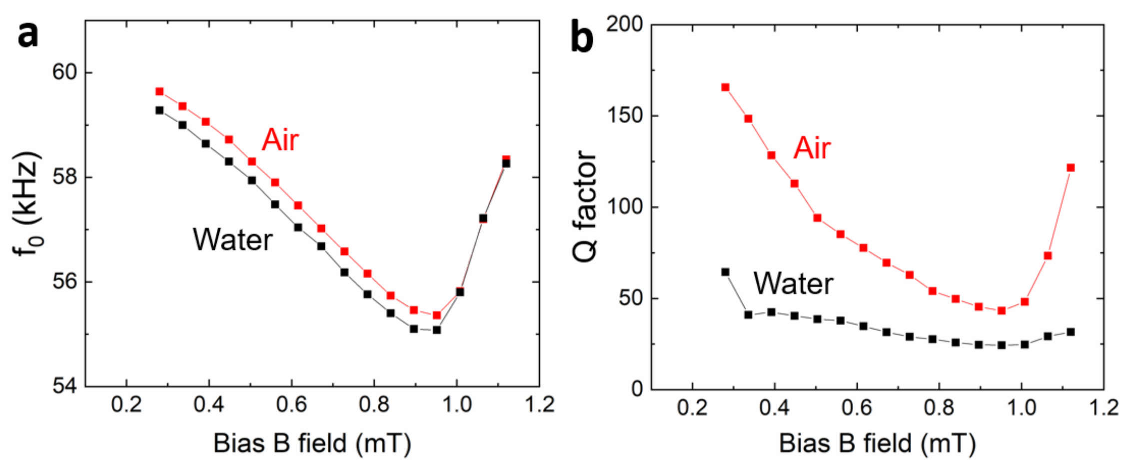

Figure S2. a) The resonance frequency of the magnetostrictive sensor at different dc bias fields at room temperature. b) Q-factor of the magnetostrictive sensor in air and water at different bias fields. Q-factor was calculated using the ratio of resonance frequency to the full-width half maximum of the resonance curve.

*email: sanjiv@illinois.edu

Thermo-magneto-mechanical model:

The following equations represent the 1D constitutive relations between the strain (ϵ), magnetization (M), and the applied magnetic field (H). We modify previously reported constitutive relations [1] to include the temperature dependence for Young's modulus at magnetic saturation (E_s).

$$\epsilon = \frac{\sigma}{E_s(1+\gamma\Delta T)} + \alpha\Delta T - \frac{\lambda_s \beta \Delta T M^2}{M_S^2} + \begin{cases} \lambda_s \tanh\left(\frac{\sigma}{\sigma_s}\right) + \frac{\left(1-\tanh\left(\frac{\sigma}{\sigma_s}\right)\right)\lambda_s M^2}{M_S^2}, & \frac{\sigma}{\sigma_s} \geq 0 \\ \frac{\lambda_s}{2}\tanh\left(\frac{2\sigma}{\sigma_s}\right) + \frac{\left(2-\tanh\left(\frac{2\sigma}{\sigma_s}\right)\right)\lambda_s M^2}{2M_S^2}, & \frac{\sigma}{\sigma_s} < 0 \end{cases} \tag{S1}$$

$$M = M_S^T \left(\coth\left(\frac{3\chi H_{eff}}{M_S^T}\right) - \frac{M_S^T}{3\chi H_{eff}}\right) \tag{S2}$$

$$M_S^T = M_S \sqrt{\frac{\left(1 - \frac{\Delta T + T_r}{T_C}\right)}{\left(1 - \frac{T_r}{T_C}\right)}} \tag{S3}$$

$$H_{eff} = H - \frac{2\lambda_s \beta \Delta T \sigma M}{\mu_0 M_S^2} + \begin{cases} \frac{\left[2\sigma - 2\sigma_S \ln\left(cosh\left(\frac{\sigma}{\sigma_S}\right)\right)\right]\lambda_s M}{\mu_0 M_S^2}, & \frac{\sigma}{\sigma_s} \geq 0 \\ \frac{\left[4\sigma - \sigma_S \ln\left(cosh\left(\frac{2\sigma}{\sigma_S}\right)\right)\right]\lambda_s M}{2\mu_0 M_S^2}, & \frac{\sigma}{\sigma_s} < 0 \end{cases} \tag{S4}$$

Where,

ϵ is the strain in the magnetostrictive material,

M is the magnetization of the magnetostrictive material,

M_S is the saturation magnetization at room temperature,

M_S^T is the saturation magnetization at a temperature T,

λ_S is the saturation magnetostrictive strain at room temperature,

H is the applied magnetic field,

H_{eff} is the effective applied magnetic field,

χ is the magnetic susceptibility of the magnetostrictive material,

σ is the compressive film stress,

σ_S is the stress at which magnetostrictive strain λ=λ_S (ref),

ΔT is the change in temperature from a room temperature of 25°C,

T_r is the reference or room temperature,

T_C is the Curie temperature,

α is the thermal coefficient of expansion, which is given by $\alpha = \frac{1}{L}\frac{dL}{dT}$,

β is the temperature coefficient of the magnetostrictive strain (λ), which is given by $\beta = -\frac{1}{\lambda}\frac{d\lambda}{dT}$,

γ is the temperature coefficient of the Young's modulus at magnetic saturation (E_S),

μ_0 is the vacuum permeability.

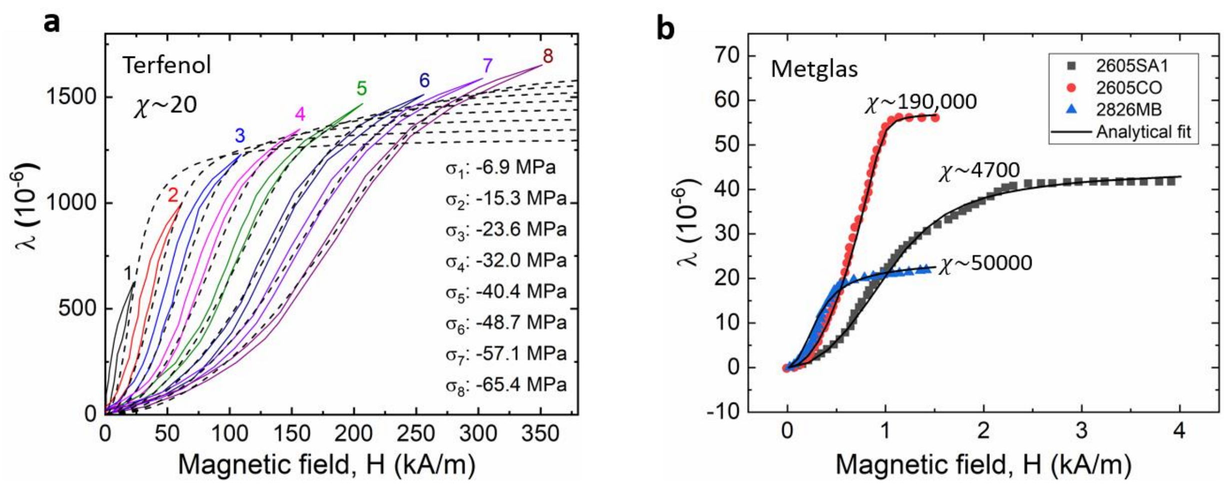

Figure S3. a) Magnetostrictive strain (λ) of Terfenol rods are shown for different bias fields and compressive stresses. The solid lines correspond to previously published experimental data, whereas the dashed lines represent our analytical fit. No fitting parameters were used. The material properties and experimental data we used can be found in Refs. [1]–[3]. b) Magnetostrictive strain (λ) of Metglas rods are shown for different bias fields. Dots represent experimental points from previous reports [4]–[6]. Solid lines represent our analytical fits. The extracted susceptibility (χ) values are shown in the graph. The corresponding fitted stress (σ) values were 18 MPa, 28 MPa, 25 MPa for 2826, 2605SA, 2605CO, respectively. Other material properties can be found in [5]–[13]. The magnetic susceptibility (χ) is dependent on the annealing conditions [14]–[16], and the obtained susceptibilities from the fit are within the expected order of magnitude based on previous reports [5]–[13].

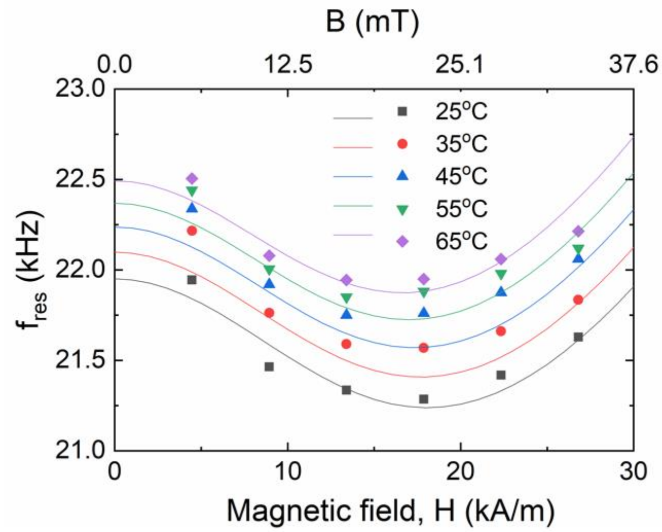

Figure S4. The resonance frequency of Terfenol rod at different temperatures and dc bias fields. The dots represent our experimental data points. The solid lines are representative of the fitting from both the analytical model and finite element simulations separately. The extracted fitting parameters were: E_S=72 MPa, γ=4.2×10^{-3} K^{-1}, β=10^{-3} K^{-1}, λ_S=800 ppm, σ=1 MPa, σ_S=30 MPa, T_C= 380°C, M_S=1.2 T, χ=25, ρ= 9200 kg/m^3. The material parameters used for fitting are in close agreement within an order of magnitude of previously reported values [1]–[3]. Any deviation could be attributed to the use of a thin layer (5 µm) of Parylene that we deposited on the Terfenol laminates to prevent corrosion.

Fitting parameters:

For Figure 6 of the manuscript:

Fit parameters:
E_S=84 MPa,
γ=-3.6×10^{-4} K^{-1}, β=1.4×10^{-3} K^{-1},
λ_S=18 ppm,
σ=17 MPa, σ_S=17 MPa,
T_C= 395°C,
M_S=1 T,
χ=50000,
ρ=7900 kg/m^3.
The fit material parameters (E_S, γ, β, λ_S, T_C, M_S, χ, ρ) are in good agreement within an order of magnitude of previously reported values [5]–[13]. The stress values (σ, σ_S) were the only other fit parameters, and they strongly depend on the sensor strip fabrication process. They are typically measured through a stress (σ) vs. magnetostrictive strain curve (λ) [17] and are not known a priori for our magnetostrictive samples.

For Figure 7 of the manuscript:

Electrical circuit fit parameters: R_e=1 Ω, L^S=0.27 mH (these are in good agreement with the measured values for the ac coil used in the experiment)

Kinematic circuit fit parameters: R=5400 N.m^{-1}s, M=0.3 N.m^{-1}s^2, C^H=28 N^{-1}m, θ=0.09 N.A^{-1}; for finite element simulations: Θ=26, ξ= 0.018 (damping factor).

Supplementary References:

[1] X. J. Zheng and L. Sun, “A nonlinear constitutive model of magneto-thermo-mechanical coupling for giant magnetostrictive materials,” *Journal of Applied Physics*, vol. 100, no. 6, p. 063906, Sep. 2006, doi: 10.1063/1.2338834.

[2] “Terfenol-D - ETREMA Products, Inc.,” *TdVib, LLC*. http://tdvib.com/terfenol-d/ (accessed Aug. 21, 2020).

[3] M. B. Moffett, A. E. Clark, M. Wun-Fogle, J. Linberg, J. P. Teter, and E. A. McLaughlin, “Characterization of Terfenol-D for magnetostrictive transducers,” *The Journal of the Acoustical Society of America*, vol. 89, no. 3, pp. 1448–1455, Mar. 1991, doi: 10.1121/1.400678.

[4] A. E. Clark and M. Wun-Fogle, “A new method of magnetostrictivity and magnetostriction measurement,” *IEEE Transactions on Magnetics*, vol. 25, no. 5, pp. 3611–3613, Sep. 1989, doi: 10.1109/20.42378.

[5] J. Zhai, S. Dong, Z. Xing, J. Li, and D. Viehland, “Giant magnetoelectric effect in Metglas/polyvinylidene-fluoride laminates,” *Appl. Phys. Lett.*, vol. 89, no. 8, p. 083507, Aug. 2006, doi: 10.1063/1.2337996.

[6] M. H. Kim, K. S. Lee, and S. H. Lim, “Magnetostriction measurements of metallic glass ribbon by fiber-optic Mach–Zehnder interferometry,” *Journal of Magnetism and Magnetic Materials*, vol. 191, no. 1, pp. 107–112, Jan. 1999, doi: 10.1016/S0304-8853(98)00310-2.

[7] A. P. Thomas and M. R. J. Gibbs, “Anisotropy and magnetostriction in metallic glasses,” *Journal of Magnetism and Magnetic Materials*, vol. 103, no. 1, pp. 97–110, Jan. 1992, doi: 10.1016/0304-8853(92)90242-G.

[8] “Materials from Metglas®, Inc.,” *Metglas, Inc.* https://metglas.com/magnetic-materials/ (accessed Aug. 21, 2020).

[9] R. Schulz, N. Alexandrov, J. Tétreault, R. Simoneau, and R. Roberge, “Development and application of amorphous core-distribution transformers in Québec,” *JMEP*, vol. 4, no. 4, pp. 430–434, Aug. 1995, doi: 10.1007/BF02649303.

[10] G. H. Hayes, W. A. Hines, D. P. Yang, and J. I. Budnick, “Low field magnetic anisotropy in Metglas 2605 CO ribbons,” *Journal of Applied Physics*, vol. 57, no. 8, pp. 3511–3513, Apr. 1985, doi: 10.1063/1.335044.

[11] B. Kundys, Y. Bukhantsev, H. Szymczak, M. R. J. Gibbs, and R. Zuberek, “Temperature dependence of saturation magnetostriction measured for Fe81Si3.5B13.5C2 amorphous films by a bending method based on the Villari effect,” *J. Phys. D: Appl. Phys.*, vol. 35, no. 11, pp. 1095–1098, May 2002, doi: 10.1088/0022-3727/35/11/301.

[12] Z. Turgut, H. Kosai, T. Bixel, J. Scofield, S. L. Semiatin, and J. Horwath, “Hysteresis loss analysis of soft magnetic materials under direct current bias conditions,” *Journal of Applied Physics*, vol. 117, no. 17, p. 17A508, May 2015, doi: 10.1063/1.4919228.

[13] S. R. Green and Y. B. Gianchandani, “Wireless Magnetoelastic Monitoring of Biliary Stents,” *Journal of Microelectromechanical Systems*, vol. 18, no. 1, pp. 64–78, Feb. 2009, doi: 10.1109/JMEMS.2008.2008568.

[14] M. Brouha and J. van der Borst, “The effect of annealing conditions on the magneto-mechanical properties of Fe-B-Si amorphous ribbons,” *Journal of Applied Physics*, vol. 50, no. B11, pp. 7594–7596, Nov. 1979, doi: 10.1063/1.326769.

[15] A. Houzali, F. Alves, J. C. Perron, and R. Barrué, “A new technique for dynamic annealing of amorphous alloys using Joule effect with controlled mechanical tensile stress,” *Review of Scientific Instruments*, vol. 66, no. 9, pp. 4671–4675, Sep. 1995, doi: 10.1063/1.1145305.

[16] M. Mouhamad, C. Elleau, F. Mazaleyrat, C. Guillaume, and B. Jarry, “Physicochemical and Accelerated Aging Tests of Metglas 2605SA1 and Metglas 2605HB1 Amorphous Ribbons for

Power Applications," *IEEE Transactions on Magnetics*, vol. 47, no. 10, pp. 3192–3195, Oct. 2011, doi: 10.1109/TMAG.2011.2158295.
[17] X. J. Zheng and X. E. Liu, "A nonlinear constitutive model for Terfenol-D rods," *Journal of Applied Physics*, vol. 97, no. 5, p. 053901, Feb. 2005, doi: 10.1063/1.1850618.